RSC Advances

ROYAL SOCIETY OF CHEMISTRY

PAPER

View Article Online
View Journal | View Issue

Check for updates

Cite this: *RSC Adv.*, 2024, **14**, 15979

A first-principles prediction of the structural, electronic, transport and photocatalytic properties of $GaGeX_3$ (X = S, Se, Te) monolayers

Pham D. Trung *[a] and Hien D. Tong *[b]

Received 6th February 2024
Accepted 19th March 2024

DOI: 10.1039/d4ra00949e

rsc.li/rsc-advances

The discovery of new 2D materials with superior properties motivates scientists to make breakthroughs in various applications. In this study, using calculations based on density functional theory (DFT), we have comprehensively investigated the geometrical characteristics and stability of $GaGeX_3$ monolayers (X = S, Se, or Te), determining their electronic and transport properties, and some essential optical and photocatalytic properties. AIMD simulations show that these materials are highly structurally and thermodynamically stable. Notably, the $GaGeSe_3$ monolayer is a semiconductor with a band gap of 1.9 eV and has a high photon absorption coefficient of up to 1.1×10^5 cm^{-1} in the visible region. The calculated solar-to-hydrogen conversion efficiency of the $GaGeSe_3$ monolayer is 11.33%, which is relatively high compared to some published 2D materials. Furthermore, the electronic conductivity of the $GaGeSe_3$ monolayer is 790.65 cm^2 V^{-1} s^{-1}. Our findings suggest that the $GaGeSe_3$ monolayer is a new promising catalyst for the solar water-splitting reaction to give hydrogen and a potential new 2D material for electrical devices with high electron mobility.

1 Introduction

Graphene, the first 2D material discovered, has shown a great combination of superior electronic, mechanical, and thermal properties compared to bulk materials, including the quantum Hall effect, high Young's modulus, high carrier mobility at room temperature, and high thermal conductivity.[1] Following the discovery of graphene, a large-scale search has been underway in materials science to discover new 2D materials. A series of new 2D materials have been discovered, such as silicene,[2,3] germanene,[4] phosphorene,[5,6] hexagonal boron nitride (h-BN),[7] and transition-metal chalcogenides.[8–10] These 2D materials have a unique structure with a high surface-area-to-volume ratio, leading to superior chemical and physical properties compared to bulk materials.[11–13] These characteristics offer the potential to achieve outstanding performances when applied in different fields, such as electronics,[14–17] sensors,[18–20] and catalysis.[21–23]

2D chalcogenides have layered structures comprising elements of the chalcogenide group (S, Se, or Te) combined with transition-metal elements.[24,25] These materials are atomically thick with many favorable electronic and mechanical properties, making them essential research subjects in nanoelectronics, optoelectronics, sensors,[18,26] and energy conversion.[27] 2D chalcogenides are synthesized using the atomic layer deposition technique, allowing expansion of their industrial applications.[24,28] Recently, chalcogenide two-dimensional materials with two transition-metal elements have attracted substantial attention due to the ability to tailor and enrich their structural and electronic properties, which should be due to the presence of a second transition-metal element in the structure.[24,29–36]

Using first-principles calculations, Hao *et al.*[29] discovered 40 stable 2D materials of the $MGeX_3$ family (M = metallic elements, X = O, S, Se or Te), including eight ferromagnetic, 21 antiferromagnetic, and 11 ferroelectric semiconductors. The $MnGeSe_3$ and $MnGeTe_3$ monolayers are predicted to be ferromagnetic metals at room temperature. Naseri *et al.*[32] demonstrated that 2D $XSnS_3$ (X = Ga, In) monolayers with the space group $162\_P\bar{3}1m$ have high energetic, kinetic, mechanical, and thermal stability. The results of Naseri *et al.* show that the 2D $GaSnS_3$ and $InSnS_3$ monolayers show moderate band gaps (1.34 eV and 1.68 eV, respectively), good absorption of visible light, and consistent band edge positions, indicating that the 2D $GaSnS_3$ and $InSnS_3$ materials are promising photocatalysts for water splitting reactions. Research by Jalil *et al.*[37] discovered that the $CoGeSe_3$ monolayer is a promising 2D photocatalyst due to its moderate band gap (1.508 eV), suitable band edge position, good visible light absorption, and high carrier mobility. Kishore *et al.*[31] discovered new potential catalysts for the water-splitting reaction, including $CdPSe_3$ and $ZnPSe_3$ monolayers, which have low exciton binding energy (in the range of 100–600 meV), high optical absorption (up to 10^5 cm^{-1}

---

[a] *Yersin University, 27 Ton That Tung, Ward 8, Dalat City, Lam Dong Province, Vietnam. E-mail: phdtrung2018@gmail.com*

[b] *Faculty of Engineering, Vietnamese-German University, Binh Duong, Vietnam. E-mail: hien.td@vgu.edu.vn*

in the visible region), high carrier mobility with mild anisotropy and moderate external potentials to promote water splitting reactions. The results of Kishore *et al.*[31] and Jalil *et al.*[37] opened up a new solution to promote energy conversion applications by developing new two-dimensional catalytic materials based on elements with high reserves and low costs, to replace the currently used rare metals, such as ruthenium and iridium. However, the big challenge for this group of materials is the limited understanding of the structural characteristics, stability, and electronic, transport, and optical properties of new materials that have not yet been synthesized appropriately in practice.

In this study, *via* calculations and simulations based on density functional theory (DFT), we have comprehensively investigated the geometrical characteristics and stability of $GaGeX_3$ (X = S, Se, Te) monolayers, determining their electronic, transport, optical, and photocatalytic properties. Our results provide essential data on the fundamental properties of newly studied two-dimensional materials. In particular, in this study, we discovered the $GaGeSe_3$ monolayer as a new candidate for use as a catalyst in the solar water-to-hydrogen splitting reaction and a potential new material in electronic devices with high electron mobility.

2 Methodology

In this study, we performed DFT calculations using the open-source computer code Quantum Espresso.[38] The Perdew–Burke–Ernzerhof generalized gradient approximation (PBE-GGA) function has been used to describe the exchange-correlation potential.[39] In the optimization and density of states calculations, the k-point grid in the Brillouin zone was set to 15 × 15 × 1 according to the Monkhorst–Pack scheme. The Heyd–Scuseria–Ernzerhof hybrid functional (HSE06) was used to calibrate the electronic bands of the studied materials.[40] The van der Waals interaction was taken into account in the calculations using the DFT-D3 approach.[41] Kinetic cutoff energies were set to 500 eV. A vacuum layer of 20 Å parallel to the monolayer surface was used to avoid unwanted interactions between periodic slabs in the simulations. The convergence thresholds for force and energy in the ionic and cell optimization calculations were set to 0.01 eV $Å^{-1}$ and 10^{-6} eV, respectively. We apply density functional perturbation theory (DFPT) to calculate the phonon spectrum with the help of the PHONOPY package.[42] Phonon spectrum calculations were performed with 4 × 4 × 1 supercells of the $GaGeX_3$ (X = S, Se, Te) monolayers. The thermal stability was investigated through *ab initio* molecular dynamics (AIMD) simulations[43] at room temperature.

3 Results and discussion

3.1 Structural properties

The optimized structure of the $GaGeX_3$ (X = S, Se, Te) monolayers is shown in Fig. 1a and b. The unit cell of these structures is rhombic in shape and contains two Ga atoms, two Ge atoms, and six chalcogen (S, Se, or Te) atoms. The main structural parameters of the $GaGeX_3$ monolayers were determined after optimization calculations with the PBE functional, and are shown in Table 1. The calculated lattice parameters of the $GaGeX_3$ monolayers are equal to 6.119, 6.457, and 7 Å, respectively, which increase from the top to the bottom of the chalcogen group in the periodic table for S, Se, and Te. In addition, the Ga–X and Ge–X bond distances (X = S, Se, Te) also increase from the top to the bottom of the chalcogen group in the periodic table for S, Se and Te ($d_{Ga-S} < d_{Ga-Se} < d_{Ga-Te}$ and $d_{Ge-S} < d_{Ge-Se} < d_{Ge-Te}$) (see Table 1). The above fact is explained by the increase in the covalent radii of the chalcogen elements in the order $r_S < r_{Se} < r_{Te}$ (by 1.05, 1.20, and 1.38 Å, respectively[44]) and the decrease in their electronegativity according to order $\mu_S > \mu_{Se} > \mu_{Te}$ (corresponding to 2.58, 2.55 and 2.1, respectively).[45]

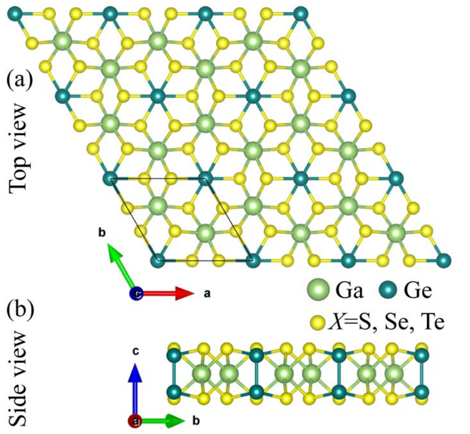

Fig. 1 The structural model of the $GaGeX_3$ (X = S, Se, Te) monolayers: (a) top view, (b) side view.

Table 1 The lattice parameters, *a* (Å), bond lengths, *d* (Å), thicknesses, *h* (Å), and cohesive energies, E_{coh} (eV per atom), of the $GaGeX_3$ (X = S, Se, Te) monolayers

	a	d_{Ga-X}	d_{Ge-X}	$d_{Ge_1-Ge_2}$	h	E_{coh}
$GaGeS_3$	6.119	2.244	2.531	2.347	3.195	4.412
$GaGeSe_3$	6.457	2.390	2.670	2.388	3.383	4.024
$GaGeTe_3$	7	2.605	2.884	2.445	3.636	3.589

Next, we investigated the structural stability of $GaGeX_3$ (X = S, Se, Te) monolayers by evaluating their energetic, mechanical, dynamical, and thermal stability. In particular, energetic stability is evaluated through the cohesive energy (E_{coh}) per atom, which is the average energy (over the number of atoms) to separate the structure into separate atoms:

$$E_{coh} = \frac{N_{Ga}E_{Ga} + N_{Ge}E_{Ge} + N_X E_X - E_{tot}}{N_{Ga} + N_{Ge} + N_X}, \tag{1}$$

where E_{tot} denotes the total energy of the $GaGeX_3$ (X = S, Se, Te) unit cell; E_{Ga}, E_{Ge} and E_X are the energies of isolated Ga, Ge, and chalcogen atoms, respectively; and N_{Ga}, N_{Ge} and N_X are the numbers of Ga, Ge, and X atoms in the $GaGeX_3$ unit cell, respectively.

The results of calculating the cohesive energies of the $GaGeX_3$ (X = S, Se, Te) monolayers are 4.412, 4.024, and 3.589 eV per atom, respectively. These values are all positive, which allows the prediction that the $GaGeX_3$ (X = S, Se, Te) monolayer structures are energetically stable. Furthermore, it is known that E_{coh} is a quantity that characterizes the strength of the bonds between atoms in a material. The greater the cohesive energy, the stronger the bonding force between atoms in the material, which is the basis for the material's mechanical strength. In comparison with previously synthesized 2D materials, we find that the cohesive energies of the $GaGeX_3$ (X = S, Se, Te) monolayers are smaller than those of the MoS_2 monolayer (5.02 eV per atom), h-BN monolayer (7.07 eV per atom),[46] and graphene (7.85 eV per atom).[47] However, the cohesive energies of the $GaGeX_3$ (X = S, Se, Te) monolayers are significantly higher than those of germanene (3.26 eV per atom)[48] and phosphorene (3.47 eV per atom).[6] These values demonstrate the relatively high motional stability of the studied 2D materials.

We calculated the phonon dispersions to evaluate the dynamical stability of the $GaGeX_3$ (X = S, Se, Te) monolayers, as shown in Fig. 2a. Negative frequencies are absent in the phonon curves of all three materials studied (Fig. 2a). This fact confirms the dynamical stability of the $GaGeX_3$ (X = S, Se, Te) monolayers.

The thermal stability of the $GaGeX_3$ (X = S, Se, Te) monolayers was evaluated through AIMD simulations. The variation in the total energy over time for the $GaGeX_3$ (X = S, Se, Te) monolayers at room temperature is shown in Fig. 2b. It can be seen that the fluctuation in the total energy of the $GaGeX_3$ (X = S, Se, Te) unit cells is negligible over the simulation period of 10 ps, indicating the high stability of the structure studied at room temperature.

Table 2 The calculated elastic constants (C_{11}, C_{12} and C_{66}), Young's moduli (Y^{2D}, in N m^{-1}), and Poisson's ratios (ν^{2D}) of the $GaGeX_3$ (X = S, Se, Te) monolayers

	C_{11}	C_{12}	C_{66}	Y^{2D}	ν^{2D}
$GaGeS_3$	83.692	27.287	28.202	74.795	0.326
$GaGeSe_3$	70.415	24.011	23.202	62.227	0.341
$GaGeTe_3$	53.92	19.384	17.268	46.952	0.36

To evaluate the mechanical stability, we use Born's stability criteria for various crystal systems, as clarified in the study of Mouhat *et al.*[49] Specifically, 2D hexagonal structures have mechanical stability when meeting the following conditions: $C_{11} > 0$ and $C_{11}{}^2 > C_{12}{}^2$.[49] The calculated elastic coefficients, as shown in Table 2, show complete satisfaction of the above conditions, confirming the mechanical stability of the $GaGeX_3$ (X = S, Se, Te) monolayers. In addition, the Poisson's ratios of the $GaGeS_3$, $GaGeSe_3$, and $GaGeTe_3$ monolayers are equal to 0.33, 0.34, and 0.36, respectively, indicating the structural flexibility of these materials under the influence of transverse deformation. These values are also significantly greater than those for graphene (0.19),[50] the MoS_2 monolayer (0.26), and the GaSe monolayer (0.25),[51] indicating more flexibility than graphene and the MoS_2 and GaSe monolayers. Furthermore, with the same uniaxial strain (x or y) applied to the three materials studied, the most significant contraction was found in the structure of the $GaGeTe_3$ monolayer in the direction perpendicular to the applied strain. This fact shows that the $GaGeTe_3$ monolayer is more sensitive to horizontal uniaxial deformations than the other two materials.

To examine the mechanical properties of the monolayers, we calculated the Young's moduli and Poisson's ratios in different directions on their horizontal planes, as shown in Fig. 3a and b.

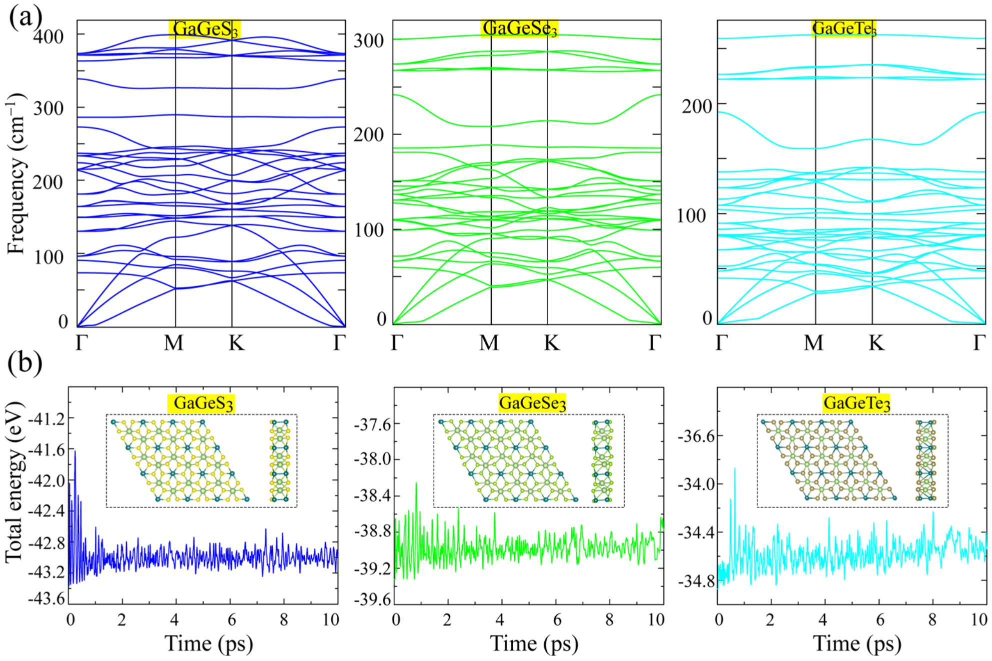

Fig. 2 (a) The phonon dispersions of the $GaGeX_3$ (X = S, Se, Te) monolayers and the energy fluctuations of the $GaGeX_3$ (X = S, Se, Te) unit cells during AIMD simulations at 300 K. (b) The energy fluctuations of the $GaGeX_3$ (X = S, Se, Te) unit cells during AIMD simulations at 300 K.

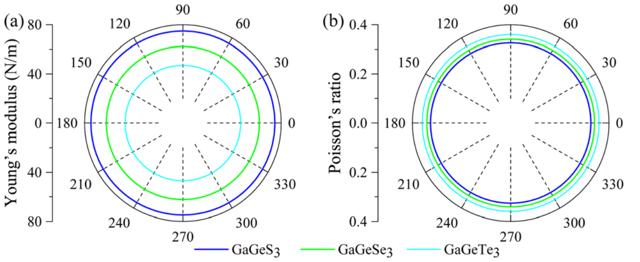

Fig. 3 The (a) Young's modulus and (b) Poisson's ratio in the *xy*-plane of the GaGeX$_3$ (X = S, Se, Te) monolayers.

It can be seen that the Young's modulus and Poisson's ratio do not change at all at different angles on the *xy*-horizontal plane, indicating isotropy in the *xy*-plane in terms of their mechanical properties.

3.2 Electronic properties

Examination of the band structures shows that the studied monolayers are all indirect semiconductors. The band gaps, calculated based on PBE, of GaGeS$_3$, GaGeSe$_3$, and GaGeTe$_3$ are 1.61, 1.124, and 0.549 eV, respectively. However, the PBE method often results in band-gap calculations that are significantly smaller than the experimental results.[41] Meanwhile, the HSE06 functional[40] is known to provide band-gap results that are more similar to those from experiments than those from the PBE method are. Therefore, we have additionally calculated the band structures of the GaGeS$_3$, GaGeSe$_3$, and GaGeTe$_3$ monolayers using the HSE06 functional, as shown in Fig. 4 compared with the PBE functional results. The band gaps of the GaGeS$_3$, GaGeSe$_3$, and GaGeTe$_3$ monolayers from the HSE06 functional are 2.511, 1.908, and 1.109 eV, respectively. The projected bands of these monolayers (Fig. 5) show that the valence band maximum (VBM) of the GaGeS$_3$, GaGeSe$_3$, and GaGeTe$_3$ monolayers is mainly formed by the hybridization of the Ge-4s orbitals and the outermost orbital (p) of the chalcogen atoms (S, Se, and Te). The participation of the Ga-4p orbital is insignificant. Meanwhile, the conduction band minimum (CBM) of these 2D materials is formed by the hybridization of Ga-4s and Ge-4s orbitals, and s and p orbitals of the chalcogen atoms (S, Se, and Te) (Fig. 5).

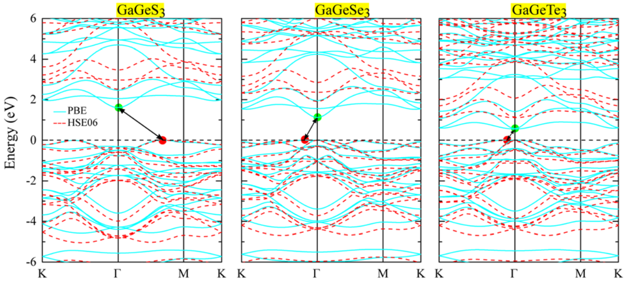

Fig. 4 Band structures of the GaGeS$_3$, GaGeSe$_3$, and GaGeTe$_3$ monolayers, calculated using PBE/HSE06 methods (cyan/red curves, respectively).

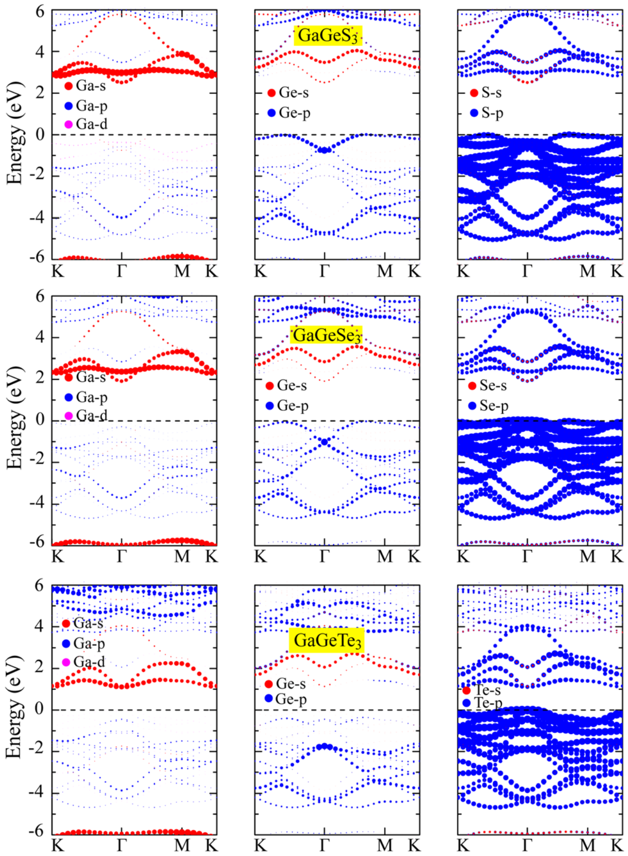

Fig. 5 Projected bands of the GaGeS$_3$, GaGeSe$_3$, and GaGeTe$_3$ monolayers using the HSE06 hybrid functional.

It can be seen that the PBE and HSE06 approximations both give similar results regarding the CBM and VBM positions of the GaGeS$_3$, GaGeSe$_3$, and GaGeTe$_3$ monolayers. The CBM of all three materials is set at the *Γ*-point, whereas their VBMs are different. Specifically, the VBM of GaGeS$_3$ is located on the line connecting the *Γ*–*M* points, while the VBMs of the other two materials are located on the line connecting *K*–*Γ* points in the Brillouin zone.

3.3 Transport properties

The carrier mobility was determined to consider the potential applications in electronic devices. The smaller mass of charged particles allows them to move faster depending on the exact value of the external electric field. High mobility of charge carriers in materials is essential for electronic applications.[52] The carrier mobility is calculated with the DP method.[53] The carrier mobility of 2D materials is calculated according to the formula:

$$\mu_{2D} = \frac{e\hbar^3 C_{2D}}{k_B T m^* \bar{m}^* {E_d}^2}, \qquad (2)$$

in which e, $\hbar$ and C_{2D} denote the electron charge, reduced Planck's constant, and 2D elastic modulus, respectively; k_B, T, m^*, $\bar{m}^*$, and E_d denote the Boltzmann constant, temperature, carrier effective mass, average effective mass, and deformation potential (DP) constant, respectively. The temperature is set to 300 K. The carrier effective mass m^* is calculated *via* parabolic fitting for the VBM and CBM according to the formula:

$$m^* = \left| \hbar^2 \left(\frac{\partial^2 E(k)}{\partial k^2} \right)^{-1} \right|, \tag{3}$$

where k and $E(k)$ are the wave vector and the energy dispersion, respectively.

The 2D elastic modulus (C_{2D}) and DP constant (E_d) are calculated according to the formulas:

$$C_{2D} = \frac{1}{\Omega_0} \frac{\partial^2 E_{tot}}{\partial {\varepsilon_{uni}}^2}, \tag{4}$$

$$E_d = \frac{\Delta E_{edge}}{\varepsilon_{uni}}, \tag{5}$$

where E_{tot} and ΔE_{edge} are the total energy and band-edge energy, respectively, of the supercell subjected to applied uniaxial strain ε_{uni}. Ω_0 is the optimized supercell area.

Here, we have calculated the effective mass (m^*), elastic modulus (C_{2D}), deformation potential (E_d), and carrier mobility (μ_{2D}) of the investigated 2D materials along the x- and y-axes, as presented in Table 3. The calculated data in Table 3 show that the carrier mobility of electrons in $GaGeS_3$ and $GaGeSe_3$ is much higher than that of holes. The carrier mobility of the holes of all three 2D structures is approximately equal along the x-and y-axis, indicating the directionally isotropic nature of the electron transport properties. However, for holes, the carrier mobilities of $GaGeS_3$, $GaGeSe_3$, and $GaGeTe_3$ along the x-axis are 1.8, 5.5, and 7.4 times larger than those along the y-axis, indicating high anisotropy of the hole transport. Notably, $GaGeSe_3$ has a high electron mobility of 790.65 $cm^2\ V^{-1}\ s^{-1}$, much higher than those of monolayer MoS_2 (200 $cm^2\ V^{-1}\ s^{-1}$),[54] MoSSe (52.7 $cm^2\ V^{-1}\ s^{-1}$),[55] and WSSe (125 $cm^2\ V^{-1}\ s^{-1}$).[56] These results demonstrate that the $GaGeSe_3$ monolayer is a potential material for application in electronic devices.

3.4 Photocatalytic properties

For this section, we have investigated some optical properties of the studied monolayer materials, thereby considering their applicability as photocatalysts. It should be noted that the necessary criteria for a photocatalyst in the reaction of splitting water into H_2 and O_2 include:[57–59]

(1) The band gap needs to be greater than 1.23 eV. This lower limit of the band gap of a photocatalyst is equal to the difference between the potential energy to produce H^+ from H_2 (−4.44 eV) and the potential energy to produce oxygen from water (−5.67 eV).[60] However, a large band gap leads to loss of the ability to convert the energy of photons with energies less than the band gap into energy for stimulating the water-splitting reaction. Related to this issue, Ran *et al.*[61] recommend that the optimal band gap for photocatalysts is about 2.0 eV to balance the requirements between chemical kinetics and light absorption to achieve an effective and high photocatalytic performance for the whole process.

(2) The CBM must be more positive than the water oxidation potential (to produce H_2 in the water oxidation reaction), and the VBM must be more negative than the H_2O reduction potential (to produce O_2 in the dehydration reaction).

(3) A proficient catalytic material should exhibit good absorption capabilities in either the visible or infrared regions, as these two regions collectively represent approximately 43%[62] and 51%[63] of the solar energy reaching Earth, respectively.

From Fig. 6b, it can be seen that the CBM positions of both the $GaGeS_3$ and $GaGeSe_3$ monolayers are higher than the required reduction potential to produce hydrogen. Meanwhile, their VBM positions are lower than the oxidation potential necessary to generate oxygen. Therefore, it is expected that $GaGeS_3$ and $GaGeSe_3$ monolayers will be able to stimulate the generation of hydrogen and oxygen from water. For the $GaGeTe_3$ monolayer, only its CBM position is suitable to produce hydrogen gas. To clarify the fulfillment of the third criterion above, we calculated the optical absorption coefficients of all three materials according to the formula:

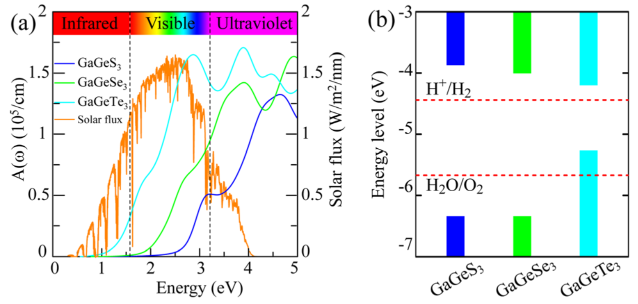

Fig. 6 (a) The optical absorption spectra of the $GaGeS_3$, $GaGeSe_3$, and $GaGeTe_3$ monolayers at the HSE06 level, compared with solar flux; (b) the band alignments of the studied monolayers in comparison with the oxidation and reduction potentials of water.

Table 3 The effective masses, m^* (m_0), elastic moduli, C_{2D} (N m^{-1}), deformation potentials, E_d (eV), and carrier mobilities, μ_{2D} ($cm^2\ V^{-1}\ s^{-1}$) along the x-and y-directions for the investigated 2D materials $GaGeX_3$ (X = S, Se, Te)

		m^*_x	m^*_y	$C_{2D}{}^x$	$C_{2D}{}^y$	$E_d{}^x$	$E_d{}^y$	$\mu_{2D}{}^x$	$\mu_{2D}{}^y$
Electrons	$GaGeS_3$	0.19	0.19	54.97	54.96	−11.35	−11.36	246.02	254.84
	$GaGeSe_3$	0.12	0.12	46.49	46.49	−9.70	−9.71	785.15	790.65
	$GaGeTe_3$	0.55	0.49	37.06	37.04	−4.42	−4.42	142.27	158.39
Holes	$GaGeS_3$	0.96	4.70	54.97	54.96	−6.66	−4.10	13.01	6.96
	$GaGeSe_3$	0.27	1.76	46.49	46.49	−6.01	−5.55	146.69	26.55
	$GaGeTe_3$	0.60	4.70	37.06	37.04	−6.45	−6.25	18.93	2.56

$$\alpha(\omega) = \frac{\sqrt{2}\omega}{c}\left(\sqrt{\varepsilon_1{}^2(\omega) + \varepsilon_2{}^2(\omega)} - \varepsilon_1(\omega)\right)^{1/2} \tag{6}$$

where ω, α, and c are used to demonstrate the angular frequency, absorption coefficient and speed of light in a vacuum, respectively; $\varepsilon_1(\omega)$ and $\varepsilon_2(\omega)$ are the real and imaginary parts of the dielectric constant, respectively.

Fig. 6a shows the absorption coefficient's dependence on the energy of the solar spectrum. From the optical absorption spectra in Fig. 6a, it can be seen that the $GaGeTe_3$ monolayer strongly adsorbs light in all visible light regions (E_{photon} in the range of 1.63–3.26 eV) with an adsorption coefficient in the range of $0.5 \times 10^5\ \text{cm}^{-1}$ to $1.5 \times 10^5\ \text{cm}^{-1}$. The adsorption coefficient of the $GaGeTe_3$ monolayer continues to be maintained at a high level above $1.5 \times 10^5\ \text{cm}^{-1}$ in the ultraviolet region ($E_{\text{photon}} > 3.26$ eV). However, the position of the bands of the $GaGeTe_3$ monolayer (Fig. 6b) is not favorable for generating a reduction reaction that produces O_2 from H_2O, as analyzed above. The $GaGeS_3$ and $GaGeSe_3$ monolayers have lower adsorption coefficients than the $GaGeTe_3$ monolayer in the visible region. The adsorption coefficient of the $GaGeSe_3$ monolayer in the visible light region ranges from $0.1 \times 10^5\ \text{cm}^{-1}$ to $1.1 \times 10^5\ \text{cm}^{-1}$; this coefficient continues to increase strongly in the ultraviolet light region and reaches the maximum value of about $1.4 \times 10^5\ \text{cm}^{-1}$ (at a photon energy of 3.8 eV). This value of the $GaGeSe_3$ monolayer is lower than those of some other potential 2D photocatalysts, such as GeC ($2.6 \times 10^5\ \text{cm}^{-1}$),[62] arsenene ($3.01 \times 10^5\ \text{cm}^{-1}$)[63] and $MoTe_2$ ($2.90 \times 10^5\ \text{cm}^{-1}$),[64] but is more significant than those of GaS ($0.71 \times 10^5\ \text{cm}^{-1}$),[63] GaSe ($0.92 \times 10^5\ \text{cm}^{-1}$)[63] and GaN ($0.59 \times 10^5\ \text{cm}^{-1}$).[65] This characteristic, combined with meeting the first and second criteria mentioned above, suggests that the $GaGeSe_3$ monolayer is a potential photocatalyst in the water-splitting reaction into hydrogen fuel.

To further clarify the applicability of the $GaGeX_3$ (X = S, Se, Te) monolayers in the water-splitting reaction, we have calculated the Gibbs free energy of hydrogen adsorption (ΔG_H) using the formula:[66,67]

$$\Delta G_H = \Delta E_H + 0.24\ \text{eV}, \tag{7}$$

where ΔE_H is the differential hydrogen absorption energy and is determined using:

$$\Delta E_H = E_{GaGeX_3+H} - E_{GaGeX_3} - \frac{1}{2}E_{H_2} \tag{8}$$

where E_{GaGeX_3+H} is the total energy of the $GaGeX_3$ (X = S, Se, Te) monolayer with one adsorbed H atom on the surface, and E_{GaGeX_3} and E_{H_2} are the total energies of the $GaGeX_3$ (X = S, Se, Te) monolayer and the energy of an H_2 molecule, respectively.

To facilitate the hydrogen evolution reaction (HER), hydrogen atoms' reversible adsorption and desorption must have small absolute values.[68,69] The Gibbs free energies of hydrogen adsorption of the $GaGeX_3$ (X = S, Se or Te) monolayers are calculated to be lowest at site B (the top of the chalcogen atom, see Fig. 7), equal to −2.24 eV, −2.04 eV, and −1.95 eV, respectively These high negative values represent strong interactions between hydrogen atoms and the catalytic surface, limiting the release of H atoms from the catalytic surface, so they predict low water-splitting catalytic performance of these monolayers compared to some other catalysts that have been reported, such as the β-PtSSe monolayer (1.13 eV), WSSe (1.51 eV)[70] and Zn_2SeTe (1.93 eV).[71] However, the Gibbs free energy of hydrogen adsorption on 2D materials can be finely tuned by applying strain, an external electric field, or structural defects,[72,73] or changing the pH of the water.[74]

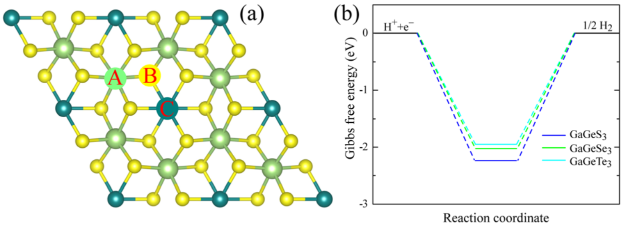

Fig. 7 (a) Different possible adsorption positions for the HER reaction on the $GaGeX_3$ (X = S, Se, Te) monolayers, (b) the calculated Gibbs free energy of the HER at the B position.

The solar-to-hydrogen (STH) conversion efficiency is known to be an important parameter for evaluating the efficiency of converting solar energy into hydrogen fuel in the water-splitting reaction. This efficiency is determined from the product of the light absorption efficiency and charge-carrier utilization:[75]

$$\eta_{\text{STH}} = \eta_{\text{abs}} \times \eta_{\text{cu}}, \tag{9}$$

The light absorption efficiency is calculated according to the formula:

$$\eta_{\text{abs}} = \frac{\int_{E_g}^{\infty} P(h\omega)\mathrm{d}(h\omega)}{\int_0^{\infty} P(h\omega)\mathrm{d}(h\omega)} \tag{10}$$

where $P(h\omega)$ is the AM1.5 G solar energy flow at photon energy $h\omega$ and E_g is the photocatalyst band gap. The numerator indicates the light power density absorbed by the photocatalyst, while the denominator is the overall power density of the reference sunshine spectrum (AM1.5G). Charge-carrier utilization (η_{cu}) is calculated according to the formula:

$$\eta_{\text{cu}} = \frac{\Delta G_{H_2O}\int_E^{\infty} \frac{P(h\omega)}{h\omega}\mathrm{d}(h\omega)}{\int_{E_g}^{\infty} P(h\omega)\mathrm{d}(h\omega)} \tag{11}$$

where ΔG_{H_2O} represents the free energy of water splitting (1.23 eV) and the remainder of the numerator indicates the effective photocurrent density. Here, E denotes the photon energy that may be used in the water-splitting process.

$$E = \begin{cases} E_g, (\chi(H_2) \geq 0.2, \chi(O_2) \geq 0.6) \\ E_g + 0.2 - \chi(H_2), (\chi(H_2) < 0.2, \chi(O_2) \geq 0.6) \\ E_g + 0.6 - \chi(O_2), (\chi(H_2) \geq 0.2, \chi(O_2) < 0.6) \\ E_g + 0.8 - \chi(H_2) - \chi(O_2), (\chi(H_2) < 0.2, \chi(O_2) < 0.6) \end{cases} \tag{12}$$

Table 4 The calculated band gap using the HSE06 method (E_g^{HSE06}), the overpotentials ($\chi(H_2)$ and $\chi(O_2)$), light absorption efficiency (η_{abs}), charge-carrier utilization (η_{Cu}) and STH conversion efficiency (η_{STH}) of the $GaGeX_3$ (X = S, Se, Te) monolayers

	E_g^{HSE06} (eV)	χ (H_2)	χ (O_2)	η_{abs} (%)	η_{Cu} (%)	η_{STH} (%)
$GaGeS_3$	2.51	0.59	0.69	17.46	42.36	7.39
$GaGeSe_3$	1.91	0.46	0.22	37.44	30.26	11.33
$GaGeTe_3$	1.11	0.26	−0.38	81.09	19.4	15.73

The band gap of the 2D materials in eqn (12) is calculated at the HSE06 level, which is known to often yield computational values closely matching experimental values.[40] The solar-energy conversion efficiencies in the water splitting reaction for the studied 2D materials, calculated using formula eqn (9), are given in Table 4.

The calculation results in Table 4 show that the light absorption efficiency (η_{abs}) and charge-carrier utilization (η_{Cu}) of the studied 2D materials have a close relationship with their band gap. Comparatively, an increase in band gap is accompanied by a decrease in light absorption efficiency and an increase in charge-carrier utilization (Table 4). The $GaGeS_3$ monolayer, featuring the most significant band gap among the studied monolayers (2.51 eV), exhibits the lowest light absorption efficiency of 17.45%. In contrast, the $GaGeTe_3$ monolayer, with the smallest band gap (1.11 eV), possesses the most significant light absorption efficiency of 81.09% and the most minor charge-carrier utilization of 19.4%. Overall, the calculated STH efficiencies of the $GaGeS_3$, $GaGeSe_3$, and $GaGeTe_3$ monolayers are 7.39%, 11.33%, and 15.73%, respectively. The calculated STH efficiency of the $GaGeTe_3$ monolayer is the largest among the studied monolayers. However, the band gap of the $GaGeTe_3$ monolayer is 1.11 eV, which is smaller than the low band gap of traditional photocatalysts.[60] Therefore, the $GaGeTe_3$ monolayer is not suitable for application as a photocatalyst in the water-splitting reaction. The STH efficiency of the $GaGeSe_3$ monolayer, equal to 11.33%, is comparable to those of some previously reported 2D photocatalysts, such as the $AgBiP_2Se_6$ monolayer (10%),[76] $Ge_2Se_2P_4$ monolayer (12.33%),[73] heptazine-based frameworks (12%),[77] and Janus WSSe monolayer (11.7%).[56] These results show that the monolayer $GaGeSe_3$ is a promising candidate as an photocatalyst in the water-splitting reaction.

4 Conclusion

In this study, we have systematically investigated the structural, electrical, transport, and notable optical and photocatalytic properties of $GaGeX_3$ (X = S, Se, Te) monolayers using DFT calculations. The AIMD simulations highlight the structural and thermodynamic stability of these 2D materials. Notably, the $GaGeSe_3$ monolayer is revealed to be a semiconductor with a band gap of 1.91 eV. In addition, it exhibits a significant photon absorption coefficient in the visible region, with a maximum value of 1.1×10^5 cm^{-1}. The calculated solar-to-hydrogen conversion efficiency of the $GaGeSe_3$ monolayer is 11.33%. The $GaGeSe_3$ monolayer's electronic conductivity has been calculated to be 790.65 cm^2 V^{-1} s^{-1}. These findings suggest that the monolayer $GaGeSe_3$ could be a promising catalyst for solar water-splitting reactions and could advance the field of electronic devices with high electron mobility.

Conflicts of interest

There are no conflicts of interest to declare.

References

1 C. Soldano, A. Mahmood and E. Dujardin, *Carbon*, 2010, **48**, 2127–2150.
2 B. Feng, Z. Ding, S. Meng, Y. Yao, X. He, P. Cheng, L. Chen and K. Wu, *Nano Lett.*, 2012, **12**, 3507–3511.
3 R. Quhe, R. Fei, Q. Liu, J. Zheng, H. Li, C. Xu, Z. Ni, Y. Wang, D. Yu and Z. Gao, *Sci. Rep.*, 2012, **2**, 853.
4 X. Li, S. Wu, S. Zhou and Z. Zhu, *Nanoscale Res. Lett.*, 2014, **9**, 1.
5 L. C. Gomes and A. Carvalho, *Phys. Rev. B: Condens. Matter Mater. Phys.*, 2015, **92**, 085406.
6 J. Guan, Z. Zhu and D. Tománek, *Phys. Rev. Lett.*, 2014, **113**, 046804.
7 K. Zhang, Y. Feng, F. Wang, Z. Yang and J. Wang, *J. Mater. Chem. C*, 2017, **5**, 11992–12022.
8 R. Fei, W. Li, J. Li and L. Yang, *Appl. Phys. Lett.*, 2015, **107**, 173104.
9 L. C. Gomes, A. Carvalho and A. C. Neto, *Phys. Rev. B: Condens. Matter Mater. Phys.*, 2015, **92**, 214103.
10 H. Wang, H. Yuan, S. Sae Hong, Y. Li and Y. Cui, *Chem. Soc. Rev.*, 2015, **44**, 2664–2680.
11 P. Ares and K. S. Novoselov, *Nano Mater. Sci.*, 2022, **4**, 3–9.
12 L. Daukiya, M. N. Nair, M. Cranney, F. Vonau, S. Hajjar-Garreau, D. Aubel and L. Simon, *Prog. Surf. Sci.*, 2019, **94**, 1–20.
13 Y. Liu, S. Zhang, J. He, Z. M. Wang and Z. Liu, *Nano-Micro Lett.*, 2019, **11**, 1–24.
14 G. Fiori, F. Bonaccorso, G. Iannaccone, T. Palacios, D. Neumaier, A. Seabaugh, S. K. Banerjee and L. Colombo, *Nat. Nanotechnol.*, 2014, **9**, 768.
15 F. Schwierz, J. Pezoldt and R. Granzner, *Nanoscale*, 2015, **7**, 8261–8283.
16 M. Huang, X. Jiang, Y. Zheng, Z. Xu, X.-X. Xue, K. Chen and Y. Feng, *Front. Phys.*, 2022, **17**, 53504.
17 T. V. Vu, B. D. Hoi, A. Kartamyshev and N. N. Hieu, *J. Appl. Phys.*, 2024, **135**, 074301.
18 N. Joshi, T. Hayasaka, Y. Liu, H. Liu, O. N. Oliveira and L. Lin, *Microchim. Acta*, 2018, **185**, 213.
19 K. D. Pham, T.-D. Hoang, Q.-T. Nguyen and D.-Q. Hoang, *J. Alloys Compd.*, 2023, **940**, 168919.
20 K. Rajkumar and R. R. Kumar, in *Gas Sensors Based on Two-Dimensional Materials and its Mechanisms*, Elsevier, 2019, pp. 205–258.
21 G. Guan, E. Ye, M. You and Z. Li, *Small*, 2020, **16**, 1907087.
22 D. Liu, A. Barbar, T. Najam, M. S. Javed, J. Shen, P. Tsiakaras and X. Cai, *Appl. Catal., B*, 2021, **297**, 120389.
23 J. Peng, X. Chen, W.-J. Ong, X. Zhao and N. Li, *Chem*, 2019, **5**, 18–50.

24 Y. Kim, W. J. Woo, D. Kim, S. Lee, S.-m. Chung, J. Park and H. Kim, *Adv. Mater.*, 2021, **33**, 2005907.

25 X. Yin, C. S. Tang, Y. Zheng, J. Gao, J. Wu, H. Zhang, M. Chhowalla, W. Chen and A. T. Wee, *Chem. Soc. Rev.*, 2021, **50**, 10087–10115.

26 X. Tang, A. Du and L. Kou, *Wiley Interdiscip. Rev.: Comput. Mol. Sci.*, 2018, **8**, e1361.

27 A. H. Reshak, *Appl. Catal., B*, 2018, **221**, 17–26.

28 H. Cai, Y. Gu, Y.-C. Lin, Y. Yu, D. B. Geohegan and K. Xiao, *Appl. Phys. Rev.*, 2019, **6**, 041312.

29 K.-R. Hao, X.-Y. Ma, H.-Y. Lyu, Z.-G. Zhu, Q.-B. Yan and G. Su, *Nano Res.*, 2021, **14**, 4732–4739.

30 T. V. Vu, H. V. Phuc, L. C. Nhan, A. I. Kartamyshev and N. N. Hieu, *J. Phys. D: Appl. Phys.*, 2023, **56**, 135302.

31 A. Kishore, H. Seksaria, A. Arora and A. De Sarkar, *Phys. Chem. Chem. Phys.*, 2023, **25**, 20337–20349.

32 M. Naseri, D. R. Salahub, T. V. Vu and H. Zakaryae, *J. Mater. Chem. C*, 2022, **10**, 11412–11423.

33 T. V. Vu, H. V. Phuc, C. V. Nguyen, V. T. Vi, A. Kartamyshev and N. N. Hieu, *Phys. Chem. Chem. Phys.*, 2022, **24**, 16512–16521.

34 R. Xiong, X. Chen, Y. Zhang, Z. Cui, J. Wen, C. Wen, J. Wang, B. Wu and B. Sa, *Langmuir*, 2023, **39**, 15837–15847.

35 Y. Zhang, Y. Shen, J. Liu, L. Lv, M. Zhou, X. Yang, X. Meng, B. Zhang and Z. Zhou, *Phys. Chem. Chem. Phys.*, 2023, **25**, 22889–22899.

36 T. V. Vu, H. V. Phuc, A. I. Kartamyshev and N. N. Hieu, *Appl. Phys. Lett.*, 2023, **122**, 061601.

37 A. Jalil, S. Z. Ilyas, S. Agathopoulos, A. Qureshi, I. Ahmed and T. Zhao, *Appl. Surf. Sci.*, 2021, **565**, 150588.

38 P. Giannozzi, S. Baroni, N. Bonini, M. Calandra, R. Car, C. Cavazzoni, D. Ceresoli, G. L. Chiarotti, M. Cococcioni and I. Dabo, *J. Condens. Matter Phys.*, 2009, **21**, 395502.

39 J. P. Perdew, K. Burke and M. Ernzerhof, *Phys. Rev. Lett.*, 1997, **78**, 1396.

40 J. Heyd, G. E. Scuseria and M. Ernzerhof, *J. Chem. Phys.*, 2003, **118**, 8207–8215.

41 S. Grimme, *J. Comput. Chem.*, 2006, **27**, 1787–1799.

42 A. Togo, L. Chaput and I. Tanaka, *Phys. Rev. B: Condens. Matter Mater. Phys.*, 2015, **91**, 094306.

43 S. Nosé, *J. Chem. Phys.*, 1984, **81**, 511–519.

44 B. Cordero, V. Gómez, A. E. Platero-Prats, M. Revés, J. Echeverría, E. Cremades, F. Barragán and S. Alvarez, *Dalton Trans.*, 2008, 2832–2838.

45 A. L. Allred, *J. Inorg. Nucl. Chem.*, 1961, **17**, 215–221.

46 Y. Luo, C. Ren, Y. Xu, J. Yu, S. Wang and M. Sun, *Sci. Rep.*, 2021, **11**, 19008.

47 L. Caputo, V.-H. Nguyen and J.-C. Charlier, *Phys. Rev. Mater.*, 2022, **6**, 114001.

48 L.-M. Yang, I. A. Popov, T. Frauenheim, A. I. Boldyrev, T. Heine, V. Bačić and E. Ganz, *Phys. Chem. Chem. Phys.*, 2015, **17**, 26043–26048.

49 F. Mouhat and F.-X. Coudert, *Phys. Rev. B: Condens. Matter Mater. Phys.*, 2014, **90**, 224104.

50 A. Politano and G. Chiarello, *Nano Res.*, 2015, **8**, 1847–1856.

51 M. Yagmurcukardes, R. T. Senger, F. M. Peeters and H. Sahin, *Phys. Rev. B*, 2016, **94**, 245407.

52 Y. Shirota and H. Kageyama, *Chem. Rev.*, 2007, **107**, 953–1010.

53 J. Bardeen and W. Shockley, *Phys. Rev.*, 1950, **80**, 72.

54 B. Radisavljevic, A. Radenovic, J. Brivio, V. Giacometti and A. Kis, *Nat. Nanotechnol.*, 2011, **6**, 147.

55 L. Ju, M. Bie, J. Shang, X. Tang and L. Kou, *J. Phys Mater.*, 2020, **3**, 022004.

56 L. Ju, M. Bie, X. Tang, J. Shang and L. Kou, *ACS Appl. Mater. Interfaces*, 2020, **12**, 29335–29343.

57 S. Nishioka, F. E. Osterloh, X. Wang, T. E. Mallouk and K. Maeda, *Nat. Rev. Methods Primers*, 2023, **3**, 42.

58 G. Wang, J. Chang, W. Tang, W. Xie and Y. S. Ang, *J. Phys. D: Appl. Phys.*, 2022, **55**, 293002.

59 D. Yao, L. Gu, B. Zuo, S. Weng, S. Deng and W. Hao, *Nanoscale*, 2021, **13**, 10624–10648.

60 J. Schneider, M. Matsuoka, M. Takeuchi, J. Zhang, Y. Horiuchi, M. Anpo and D. W. Bahnemann, *Chem. Rev.*, 2014, **114**, 9919–9986.

61 J. Ran, J. Zhang, J. Yu, M. Jaroniec and S. Z. Qiao, *Chem. Soc. Rev.*, 2014, **43**, 7787–7812.

62 K. Ren, C. Ren, Y. Luo, Y. Xu, J. Yu, W. Tang and M. Sun, *Phys. Chem. Chem. Phys.*, 2019, **21**, 9949–9956.

63 J. Li, Z. Huang, W. Ke, J. Yu, K. Ren and Z. Dong, *J. Alloys Compd.*, 2021, **866**, 158774.

64 C. Shao, K. Ren, Z. Huang, J. Yang and Z. Cui, *Front. Chem.*, 2022, **10**, 847319.

65 K. Ren, Y. Luo, J. Yu and W. Tang, *Chem. Phys.*, 2020, **528**, 110539.

66 J. K. Nørskov, T. Bligaard, A. Logadottir, J. Kitchin, J. G. Chen, S. Pandelov and U. Stimming, *J. Electrochem. Soc.*, 2005, **152**, J23.

67 F.-S. Zhang, J.-W. Wang, J. Luo, R.-R. Liu, Z.-M. Zhang, C.-T. He and T.-B. Lu, *Chem. Sci.*, 2018, **9**, 1375–1384.

68 C. Tsai, K. Chan, J. K. Nørskov and F. Abild-Pedersen, *Catal. Sci. Technol.*, 2015, **5**, 246–253.

69 Q. Wang, Z. L. Zhao, S. Dong, D. He, M. J. Lawrence, S. Han, C. Cai, S. Xiang, P. Rodriguez and B. Xiang, *Nano Energy*, 2018, **53**, 458–467.

70 P. Jamdagni, A. Kumar, S. Srivastava, R. Pandey and K. Tankeshwar, *Phys. Chem. Chem. Phys.*, 2022, **24**, 22289–22297.

71 X. Tan, Q. Chen, Y. Liang, Z. Tian, T. Gao and Q. Xie, *Int. J. Hydrogen Energy*, 2024, **51**, 222–230.

72 Z. Haman, N. Khossossi, M. Kibbou, I. Bouziani, D. Singh, I. Essaoudi, A. Ainane and R. Ahuja, *Appl. Surf. Sci.*, 2022, **589**, 152997.

73 T. V. Vu, N. N. Hieu, D. D. Vo, A. Kartamyshev, H. D. Tong, T. T. Trinh, V. Khuong Dien, Z. Haman, P. Dey and N. Khossossi, *J. Phys. Chem. C*, 2024, **128**, 4245–4257.

74 M. Jakhar and A. Kumar, *J. Mater. Chem. A*, 2022, **10**, 6785–6795.

75 C.-F. Fu, J. Sun, Q. Luo, X. Li, W. Hu and J. Yang, *Nano Lett.*, 2018, **18**, 6312–6317.

76 L. Ju, J. Shang, X. Tang and L. Kou, *J. Am. Chem. Soc.*, 2020, **142**, 1492–1500.

77 Y. Zhao, C. Wang, X. Han, Z. Lang, C. Zhao, L. Yin, H. Sun, L. Yan, H. Ren and H. Tan, *Adv. Sci.*, 2022, **9**, 2202417.